nanomaterials

MDPI

Article

Atomistic Investigation of the Titanium Carbide MXenes under Impact Loading

Kang Xia [1,2,*], Haifei Zhan [2,3,*], Xinjie Zhang [1] and Zhiyong Li [2]

[1] College of Mechanical & Electrical Engineering, HoHai University, Nanjing 210098, China; xj.zhang@hhu.edu.cn
[2] School of Mechanical, Medical and Process Engineering, Queensland University of Technology (QUT), Brisbane, QLD 4001, Australia; zhiyong.li@qut.edu.au
[3] College of Civil Engineering and Architecture, Zhejiang University, Hangzhou 310058, China
* Correspondence: xiak@hhu.edu.cn (K.X.); zhan_haifei@zju.edu.cn (H.Z.)

Abstract: 2D Titanium carbide MXenes with a structural formula recognized as $Ti_{n+1}C_n$ have attracted attention from both the academic and industry fields due to their intriguing mechanical properties and appealing potential in a variety of areas such as nano-electronic circuits/devices, bio sensors, energy storage and reinforcing material for composites. Based on mutli-body comb3 (third-generation Charge-Optimized Many-Body) potential, this work investigated the impact resistance of monolayer $Ti_{n+1}C_n$ nanosheets (namely, Ti_2C Ti_3C_2 and Ti_4C_3) under hypervelocity up to 7 km/s. The deformation behavior and the impact resist mechanisms of $Ti_{n+1}C_n$ nanosheets were assessed. Penetration energy is found to positively correlate with the number of titanium atom layer (n). However, in tracking atomic Von Mises stress distribution, Ti_2C exhibits the most significant elastic wave propagation velocity among the examined nanosheets, suggesting the highest energy delocalization rate and stronger energy dissipation via deformation prior to bond break. Consistently, Ti_2C presents superior specific penetration energy due its Young's-modulus-to-density ratio, followed by Ti_3C_2 and Ti_4C_3, suggesting an inverse correlation between the titanium atom layer number and specific penetration energy. This study provides a fundamental understanding of the deformation and penetration mechanisms of titanium carbide MXene nanosheets under impact, which could be beneficial to facilitating their emerging impact protection applications.

Keywords: titanium carbide MXene; hypervelocity impact; molecular dynamics simulation

Citation: Xia, K.; Zhan, H.; Zhang, X.; Li, Z. Atomistic Investigation of the Titanium Carbide MXenes under Impact Loading. *Nanomaterials* **2022**, *12*, 2456. https://doi.org/10.3390/nano12142456

Academic Editors: Andres Castellanos-Gomez and Werner Blau

Received: 5 June 2022
Accepted: 13 July 2022
Published: 18 July 2022

1. Introduction

The first phenomenal 2D material, graphene, is renowned for its record-breaking properties [1]. Followed by its discovery, tremendous efforts on the exploration of graphene-analogous 2D carbonaceous materials and transition metal carbides/nitrides (widely recognized as MXenes) are conducted. MXenes are 2D-layered transition metal carbon/nitride materials first realized by selectively washing out element 'A' in the atomically layered MAX phase with the etching approach [2], where 'M', 'A', 'X' represent an early transition metal, an A-group metal element (more specifically, a group IIIA or IVA element) and a C and/or N element, respectively [3]. As a classical 2D nanomaterial, a strong binding energy from the M-X valence bond leads to strong mechanical properties in MXene [4].

Titanium carbide MXenes can be represented as $Ti_{n+1}C_n$ and have received immense attention from various fields, including the civil, automobile, aerospace and military industries, owing to their superior bending rigidity [5], Young's modulus, strength-to-weight ratio [6], oil/water separation capability [7], electro-chemical performance [8], etc. To date, $Ti_{n+1}C_n$ has been realized via either top-down or bottom-up techniques. Representative top-down synthesis approaches include fluorine-based selective etching, which usually induces oxygen-containing termination functional groups. In contrast, bottom-up synthesis methods such as chemical vapor deposition can produce 'pristine'

$Ti_{n+1}C_n$, with its surface not terminated. Considering the product quality and experiment setup difficulty, the top-down approach is clearly the main stream [9,10].

Varieties of $Ti_{n+1}C_n$ have been successfully realized so far; however, constrained by the lateral size of sheets and the complex oxygen-containing function groups observed in the synthesis process, most studies on monolithic $Ti_{n+1}C_n$ are carried out via the in silico approach [10]. Deploying the empirical potential energy function and embedded atom method, the molecular dynamics (MD) study suggests that the bending rigidity of these 2D titanium carbides can be as high as ~49.55 eV, which is significantly larger than that of other popular 2D materials such as graphene and MoS_2 (whose bending rigidities are calculated to be 2.3 and 9.61 eV, respectively) [5]. A recent MD study also revealed that the Young's modulus of $Ti_{n+1}C_n$ ranges between 133 and 517 GPa, which indicates its potential usages in nano-electronics and energy storage [6]. In addition to the research on pristine $Ti_{n+1}C_n$, a density functional theory (DFT) study on functionalized $Ti_{n+1}C_n$ suggested that the oxygen group not only results in strong anisotropy but also enhances their ideal tensile strength [1].

Besides its outstanding mechanical properties, $Ti_{n+1}C_n$ is also renowned as a strengthening material/matrix in a variety of composites and facilitates applications in nanogenerators, EMI shielding and sensors. The negatively charged MXene, due to the presence of oxygen-containing functional groups, is able to form a strong interaction with positively charged polymers, which improves the interfacial strength and interfacial load transfer efficiency [11]. In fact, lamellar composites with a stronger interfacial strength possess superior mechanical properties when subjected to quasi-static loading conditions [12].

Considering the outstanding mechanical behavior of $Ti_{n+1}C_n$ under the quasi-static loading condition, its performance under impact loading is rarely discussed in the literature; however, it is critical to facilitate its application in mechanical energy storge and bullet proof-related applications [12–14]. Due to the experimental complexity and small dimensions of available MXenes sheets [12], a pilot study on their impact resistance under various impact velocities is carried out utilizing the MD method in this work, with an emphasis on its deformation process, stress distribution capability and specific penetration energy.

2. Materials and Methods

The anti-ballistic performance and fracture behavior of $Ti_{n+1}C_n$ nanosheets subject to a hypervelocity impact are examined through MD simulations utilizing the open-source package LAMMPS [15]. Diamond is considered one of the strongest materials on earth and can stand hypervelocity impacts without cracking [16–18]; thus, a projectile with a diamond lattice structure is prepared for the impacts. The projectile is made up of 11,543 carbon atoms with a spherical shape of approx. 25 Å in radius. Square $Ti_{n+1}C_n$ nanosheets with fixed boundaries (highlighted with magenta in Figure 1) have identical planar dimensions of 500 × 500 $Å^2$ (containing 95,616, 159,360 and 214,508 atoms, respectively, for n = 1 to 3) [19]. High initial velocities up to 70 Å /ps (i.e., 7 km/s) are assigned to the projectile, with its initial bottom positions ~18 $Å^2$ above the geometric center of the nanosheet. The purpose of assigning an initial velocity to a free-standing projectile is to trace its energy variation during the whole impact process [18,20,21]. For comparison, projectile energy tracing is not achievable in LAMMPS utilizing a pure force, high speed indentation setup.

In this study, the third-generation Charge-Optimized Many-Body (COMB3) potential is employed to describe the C and Ti atomic interactions within the MXene nanosheets, as it is fully optimized to determine the binding energy of carbon- and metal-based systems [22–26]. The general form of COMB3 potential is defined as follows:

$$E_{COMB3} = \sum_i [E_i^{self}(q_i) + \sum_{j>i}\left[E_{ij}^{short}(r_{ij}, q_i, q_j) + E^{Coul}(r_{ij}, q_i, q_j)\right] + E^{polar}(q_i, r_{ij}) + E^{vdW}(\{r_{ij}\}) + E^{barr}(\{r_{ij}\}) + E^{corr}\left(\left\{r_{ij}, \theta_{ijk}\right\}\right)] \quad (1)$$

where E^{self} is an electrostatic term of atom i, which is the sum of the atomic ionization energies and electron affinities. E^{SHORT} presents the bond-order potential between the

atom i and j. E^{Coul}, E^{vdW}, E^{barr} and E^{CORR} are the Coulomb, van der Waals, charge barrier function and correction energy term, respectively. E^{polar} is a term describing the polarization in an organic system which is excluded in this study. A modified Tersoff potential with a cutoff distance extended to 2.45 Å has been proven to represent the binding energy for diamond structures well [27], and it is adopted to mimic the atomic force within the diamond projectile. As the diamond projectile approaches MXene nanosheets, the 'weak' van der Walls force/interactions between the two structures are described by a Morse potential, which has been successfully used for diamond-involved contact simulation such as indentation [28,29], collision [30] and machining [31]. The general form of Morse potential is expressed as:

$$V(r_{ij}) = D\left(e^{-2\alpha(r_{ij}-r_0)} - 2e^{-\alpha(r_{ij}-r_0)}\right) \quad (2)$$

where α, D and r_0 represent range parameter, dissociation energy and equilibrium internuclear distance, respectively. The parameters in the Morse potential used for C–C interaction are: α = 2.624 Å^{-1}, D = 0.650 eV and r_0 = 2.000 Å [32]. Considering the C–Ti interaction, these three parameters are 1.900 Å^{-1}, 0.0137 eV and 2.867 Å , respectively [31].

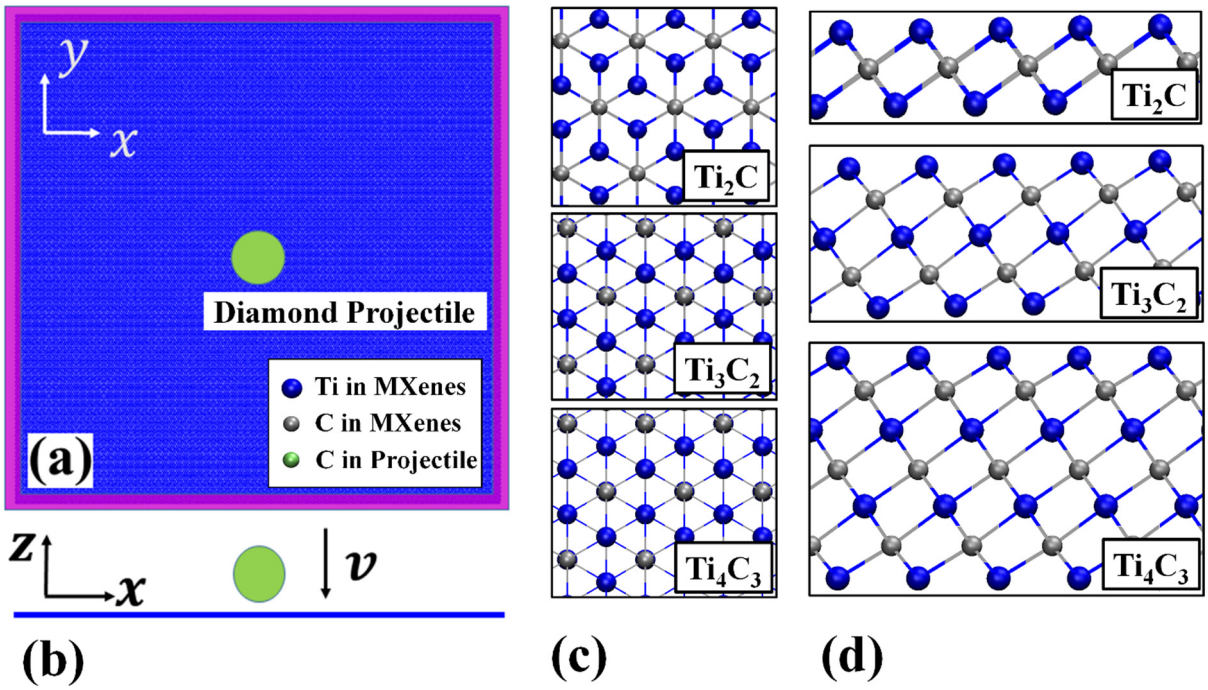

Figure 1. Impact simulation setup for Mxenes. (**a**) Top view of the sample, the magenta area indicates the fixed boundary and the green object is the diamond projectile; (**b**) Side view of the sample; (**c**,**d**) show the top and front view of the atomic structures for Ti_2C Ti_3C_2 and Ti_4C_3, respectively.

During the relaxation stage, by employing non-periodic boundary conditions, an NVT (canonical) ensemble, a conjugate gradient algorithm and a Nose–Hoover thermostat [33], the whole system is equilibrated for 4000 fs at a low environment temperature of 10 K to achieve a minimum energy state. For the impact stage, a non-periodic boundary and a small time step of 0.1 fs are selected for the simulation in order to capture the dramatic deformation of the nanosheets. A time step of 0.5 fs is also employed to validate the setup, and similar results are obtained. The equations of motion are integrated with time using a velocity Verlet algorithm [34]. Temperature has great impacts on material strength, and they are negatively correlated for most materials [35,36]. For a fair comparison, the environment temperature is set to be a low value of 10 K for all the cases (20 K and 30 K are also tested, with similar simulation results obtained), aiming to minizine the influence of high thermal fluctuations (generated via impact), which may potentially weaken the material strength. To mimic the energy conversion between the kinetic and potential energy,

the NVE (microcanonical) ensemble is chosen, and the thermostat is not applied to the system, during the entire impact stage.

The atomic stress in this work is calculated according to the virial stress $\Pi^{\alpha\beta}$, which is expressed as [37]:

$$\Pi^{\alpha\beta} = \frac{1}{\Omega}\left(-\sum_i m_i v_i^{\alpha} v_i^{\beta} + \frac{1}{2}\sum_i \sum_{j\neq i} F_{ij}^{\alpha} r_{ij}^{\beta}\right) \quad (3)$$

Here, Ω donates the volume of the structure. m_i and v_i are the mass and velocity of the i^{th} atom, respectively. F_{ij} and r_{ij} are the force and distance between atoms i and j, respectively, and the indices α and β denote the Cartesian components. The volume of the 2D $Ti_{n+1}C_n$ nanosheets is estimated by assuming them to be continuum media with different thicknesses. Adopting a different volume alters the stress calculation; however, the $Ti_{n+1}C_n$ nanosheets adopted in the work share similar lattice structures and densities. For the reason above, the volume differences will not change the trends of the results presented in this paper. Considering the complicated stress variation during impacts, Von Mises stress σ_{VM} in the $Ti_{n+1}C_n$ is traced based on the atomic virial stress tensor. The tensor for each atom used for σ_{VM} computation is a six-element vector, including three normal stresses—σ_x, σ_y, σ_z—and three planar stresses—σ_{xy}, σ_{xz}, σ_{yz}. The σ_{VM} is calculated from:

$$\sigma_{VM} = \sqrt{\left((\sigma_x - \sigma_y)^2 + (\sigma_y - \sigma_z)^2 + (\sigma_z - \sigma_x)^2 + 6(\sigma_{xy}{}^2 + \sigma_{xz}{}^2 + \sigma_{yz}{}^2)\right)/2} \quad (4)$$

Initially, the impact performance of the Ti_2C nanosheet under an impact velocity of 2 km/s is highlighted. In the vacuum environment, the total energy change in the projectile equals the energy change in the Ti_2C nanosheet. During the impact process, although the projectile experiences ignorable deformation, a notable amount of potential energy change of about 80.78 eV in the projectile ($\Delta E_{ball,pe}$) is observed (Figure 2a). After perforation, the total energy loss in the projectile ($\Delta E_{ball,tot}$), which is the sum of $\Delta E_{ball,pe}$ and $\Delta E_{ball,ke}$, remains constant (Figure 2b). Thus, $\Delta E_{ball,tot}$ is taken as the penetration energy (E_p) rather than $\Delta E_{ball,ke}$ alone [16,17].

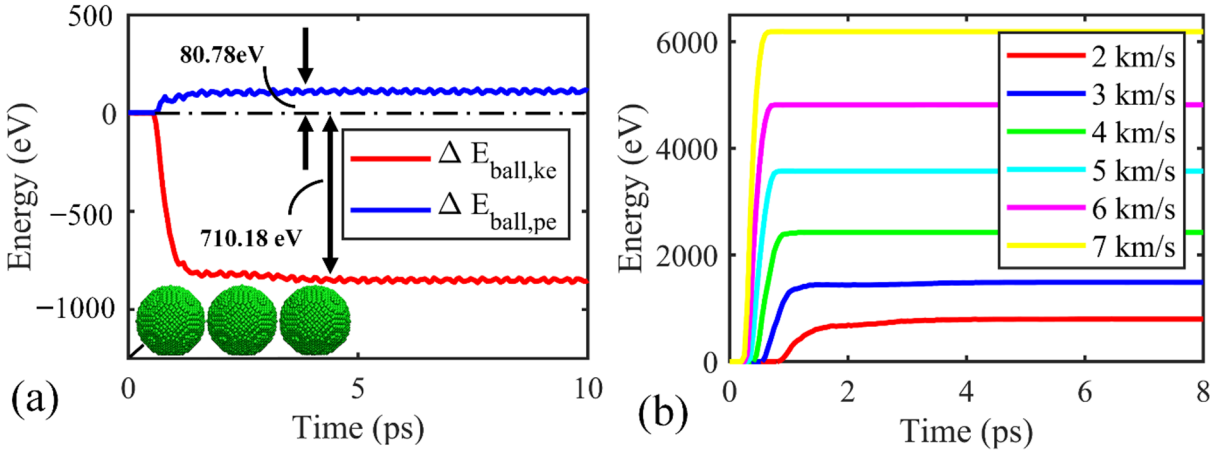

Figure 2. Energy variation over time for the projectile impact with the Ti_2C membrane. (**a**) Energy change in the projectile as a function of time for an impact velocity of 2 km/s. $\Delta E_{ball,ke}$ and $\Delta E_{ball,pe}$ represent the kinetic and potential energy change of the projectile, respectively. (**b**) Dissipated energy in the projectile ($\Delta E_{ball,tot}$) during the impact process.

3. Results and Discussion

3.1. Deformation Characteristics

To acquire the deformation process, the atomic configurations of three $Ti_{n+1}C_n$ MXenes (Ti_2C, Ti_3C_2, Ti_4C_3) under impact velocities ranging from 0.1 km/s up to 7 km/s are investigated. Figure 3 illustrates the deformation of the Ti_2C nanosheet subjected to a low impact velocity of ~0.4 km/s, and no bond break is observed during the whole impact

process. Six deformation stages can be identified, which are shown in Figure 3. The diamond projectile reaches the Ti_2C membrane at ~7.5 ps, and significant kinetic energy is transmitted to the impact region (Figure 3a,b). A maximum out-of-plane deflection of ~33.94 Å is reached at 22.5 ps (Figure 3c). The projectile remains in contact with the nanosheet for a short period and then disengages at ~37.5 ps (Figure 3d). Thereafter, the local deformation propagates to the boundary, and the nanosheet resumes to a flat status with obvious out-of-plane vibration (Figure 3e,f). Similar deformation phenomena are observed from the Ti_3C_2 and Ti_4C_3 nanosheets, though the maximum out-of-plane deflections are significantly smaller—about ~26.31 Å and ~20.01, respectively.

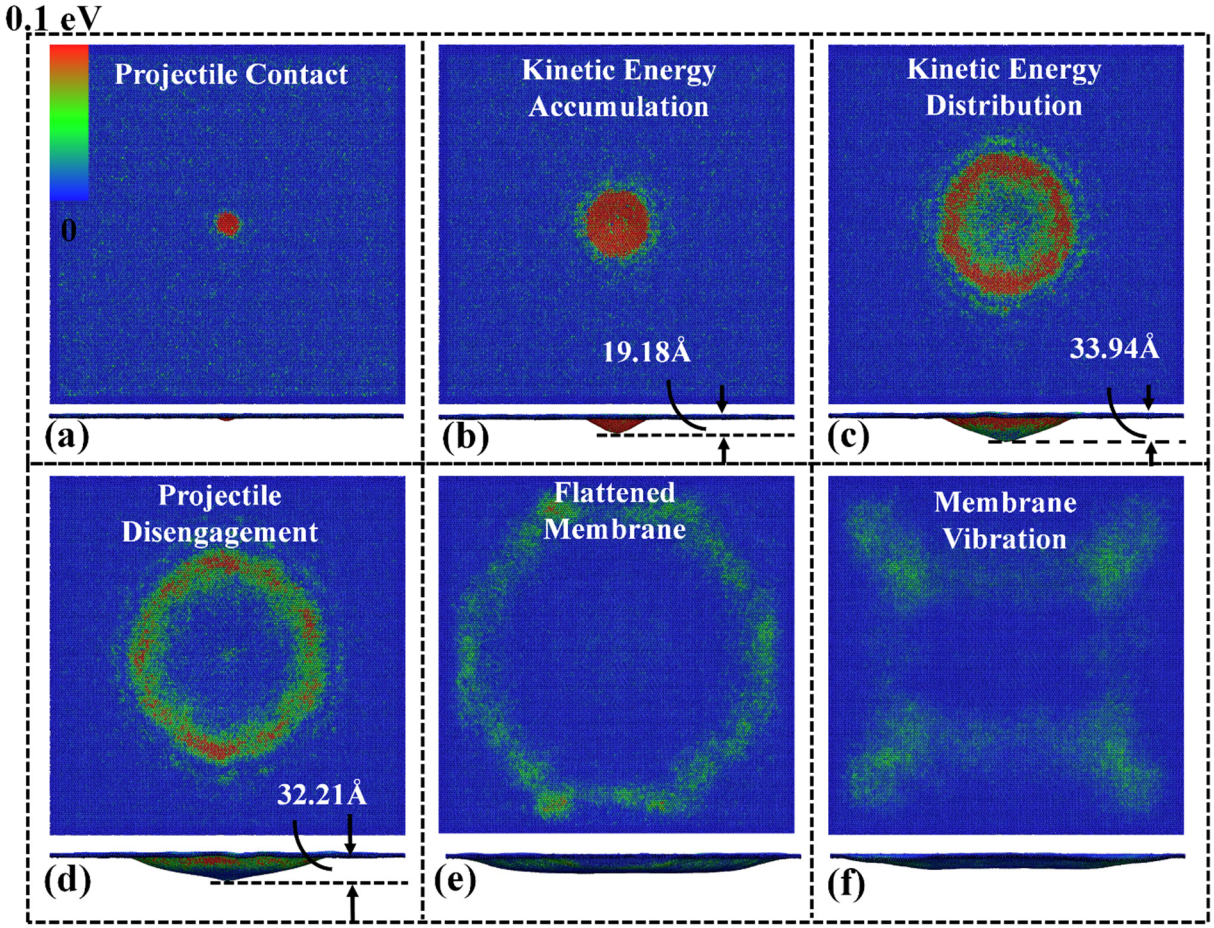

Figure 3. Impact deformation and kinetic energy distribution of the Ti_2C nanosheet under an impact velocity of 0.4 km/s. Upper panels and bottom panels are the top and side views of the nanosheets, respectively. The kinetic energy distribution at the simulation times of: (**a**) 7.5 ps; (**b**) 12.5 ps; (**c**) 22.5 ps; (**d**) 37.5 ps; (**e**) 62.5 ps; and (**f**) 102.5.

As the impact velocity increases to ~1 km/s, local damage of the nanosheets is observed for all the examined samples, and the projects are trapped in the damaged area. The perforation is observed when the velocity is increased to ~1.2, 1.4 and 1.6 km/s for the Ti_2C, Ti_3C_2 and Ti_4C_3 nanosheets, respectively. Figure 4 shows the failure scenario of the nanosheets subject to an impact velocity of 2 km/s. As can be seen, cracks initiate from the impact area with the accumulated stress, and the thinnest Ti_2C nanosheet experiences the largest out-of-plane deformation prior to the complete failure (~32.82 Å, Figure 4a) compared with the Ti_3C_2 and Ti_4C_3 counterparts (Figure 4b,c). After perforation at 5.7 ps (Figure 4d–f), more discrete debris is generated from the Ti_3C_2 and Ti_4C_3 nanosheets. As expected, the thicker nanosheet adsorbs more kinetic energy, and, thus, the projectile exhibits a shorter travel distance at the same simulation time of 5.7 ps.

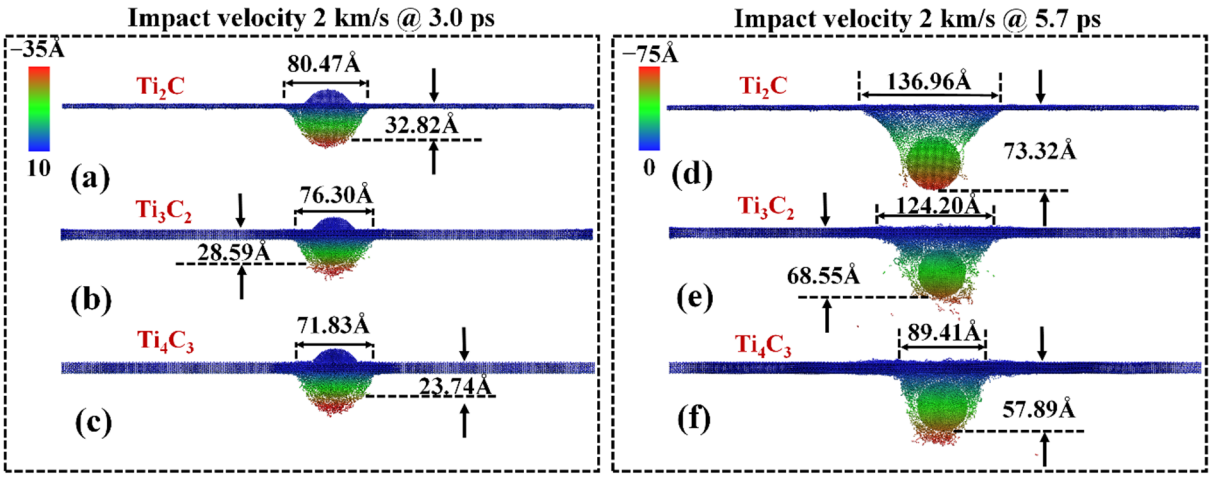

Figure 4. Side view of the z-direction deformation in $Ti_{n+1}C_n$ under an impact velocity of 2 km/s. Atomic configurations at a simulation time of 3.0 ps: (**a**) Ti_2C; (**b**) Ti_3C_2; (**c**) Ti_4C_3. Atomic configuration at a simulation time of 5.7 ps: (**d**) Ti_2C; (**e**) Ti_3C_2; (**f**) Ti_4C_3. Atoms are colored according to their coordinates in the thickness direction.

Severer local deformation is observed when the impact velocity increases further. The amount of discrete debris in nanosheets presents a positive correlation with impact velocity. Under the high impact velocity of ~5 km/s, the contact region melts immediately as the projectile reaches the nanosheet and the high impact energy creates a lot of small discrete debris for all samples. Among all three samples, Ti_4C_3 owns the largest number of atoms and, consistently, impact Ti_4C_3 leads to the largest amount of discrete debris for an impact velocity above 5 km/s (Figure 5). During the crack propagation phase, the accumulated stress (at the impact region) starts to re-distribute, and the stress distribution in the deformed region of Ti_2C and Ti_4C_3 exhibits a circular pattern (Figure 5b,f), while the Ti_3C_2 nanosheet demonstrates a hexagonal pattern (Figure 5d). This phenomenon is considered to be a result of the lattice structure and lattice orientation.

Differently from the armchair/zigzag kicking fracture mechanisms and significant crack propagation phenomena observed in carbonaceous nanosheets [17,38,39], the cracks in $Ti_{n+1}C_n$ propagate slightly along all directions. The shape and size of the damaged area are generally the same during the short crack expansion period; this phenomenon is related to $Ti_{n+1}C_n$ MXenes' metal-like, plastic deformation energy adsorption mechanism. Recall the stress-strain curve of $Ti_{n+1}C_n$—as the ultimate stress reaches locally, a total failure in MXenes is not observed immediately [40,41]. However, the stress-strain curve of carbonaceous nanosheets usually drops directly to 0 upon ultimate stress, suggesting brittle behavior, which is consistent with their large crack propagation phenomena [42]. Additional simulations conducted by using a time step of 0.1 fs to 0.5 fs yield the same observations.

3.2. Stress Distribution and Propogation

With the above deformation understanding of $Ti_{n+1}C_n$ nanosheets under impact, we then analyze the stress distribution and propagation feature within the MXenes. For the same impact velocity amplitude, the probability densities of the von Mises stress (prior to bond break) for the three MXene nanosheets share a similar unimodal distribution pattern (Figure 6a). Subjected to the same impact velocity, the thinnest Ti_2C nanosheet possesses the lowest probability density peak at a higher stress magnitude, as it experiences larger deformation prior to the bond break compared with the thicker samples.

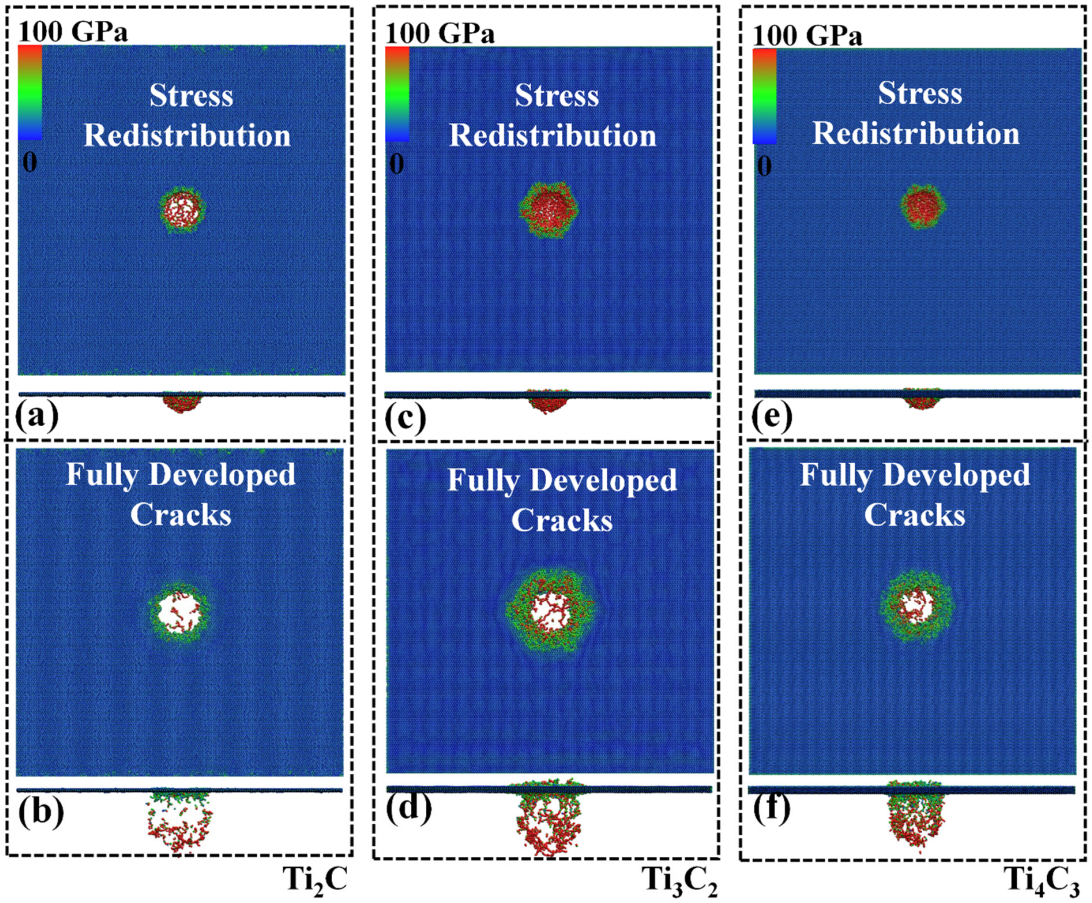

Figure 5. von Mises stress distribution of the MXene nanosheets under an impact velocity of 5 km/s. Upper panels and bottom panels are the top and side views of the nanosheets, respectively. Atomic configuration of Ti_2C nanosheets at simulation times of: (**a**) 0.7 ps and (**b**) 1.9 ps. Atomic configuration of Ti_3C_2 nanosheets at simulation times of: (**c**) 0.7 ps and (**d**) 1.9 ps. Atomic configuration of Ti_4C_3 nanosheets at simulation times of: (**e**) 0.7 ps and (**f**) 1.9 ps. For all figures, the upper panel is the top view and the lower panel is the front view.

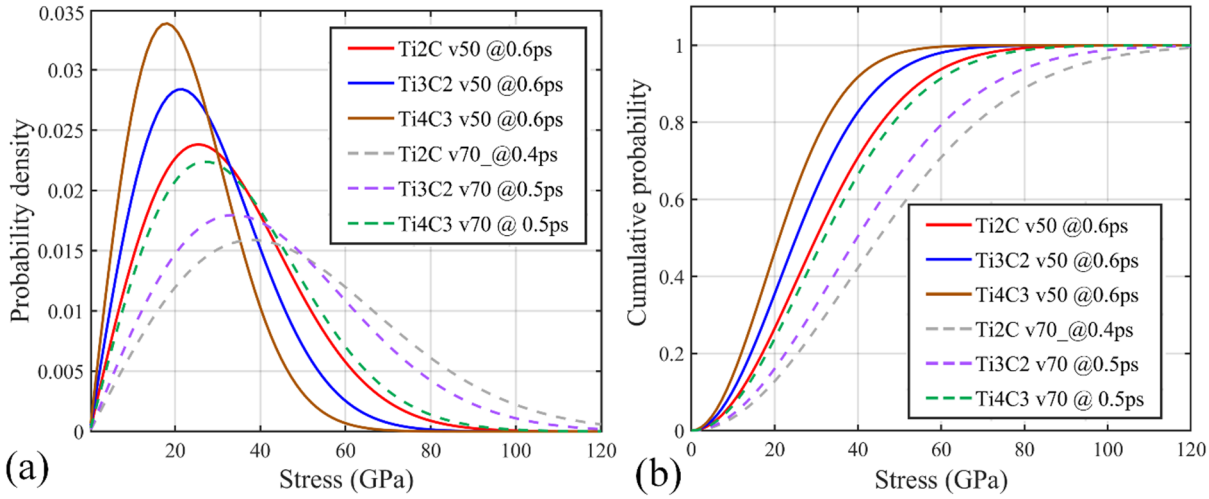

Figure 6. The distribution characteristics of the von Mises stress of $Ti_{n+1}C_n$ nanosheets under impact prior to bond break. (**a**) The probability density of the von Mises atomic stress; and (**b**) the cumulative density of the von Mises atomic stress.

As the impact velocity increases, the peak of the probability density curve for each sample declines, and its location shifts to a higher stress magnitude (dash lines in Figure 6a). Larger impact velocities result in severer stress concentrations at the impact region. Meanwhile, the melting atoms or the generation of debris adversely influence the stress propagation; therefore, the probability density profile becomes flattened at higher impact velocities. Such observation agrees well with that reported for other nanostructures [10,43].

Theoretically, the elastic stress wave velocity v_s in a solid material can be calculated based on its Young's modulus E and density ρ according to $v_s = \sqrt{E/\rho}$ [44,45]. Alternatively, v_s can be estimated by tracking the location of the highest von Mises atomic stress during the simulation [39]. According to the simulation results, the elastic wave propagation velocity along the in-plane X direction is about 10.21, 9.31 and 9.20 km/s for Ti_2C, Ti_3C_2 and Ti_2C, respectively. Along the in-plane Y direction, it is about 10.81, 9.32 and 9.11 km/s, respectively. The estimated wave velocity agrees well with the theoretical calculation based on the reported Young's modulus [4,40,41]. The cumulative density of the von Mises atomic stress prior to the bond break presented in Figure 6b also agrees well with the above finding: the curve slopes of the three materials subject to the same impact velocity suggest that Ti_2C is likely to bear more loading prior to the bond break. It also suggests that Ti_4C_3 has the least significant breaking stress among all three materials.

3.3. Impact Resistance Evaluation

To quantitatively evaluate the impact resistance of $Ti_{n+1}C_n$ nanosheets, its penetration (E_p) and specific penetration energy E_p^* under various velocity amplitudes are calculated and compared. According to Figure 7a, the penetration energies of the three 2D titanium carbide MXene nanosheets increase similarly in the examined impact velocity ranging from 2 to 7 km/s. Specifically, the Ti_4C_3 nanosheet shows the largest E_p, suggesting a stronger impact resistance.

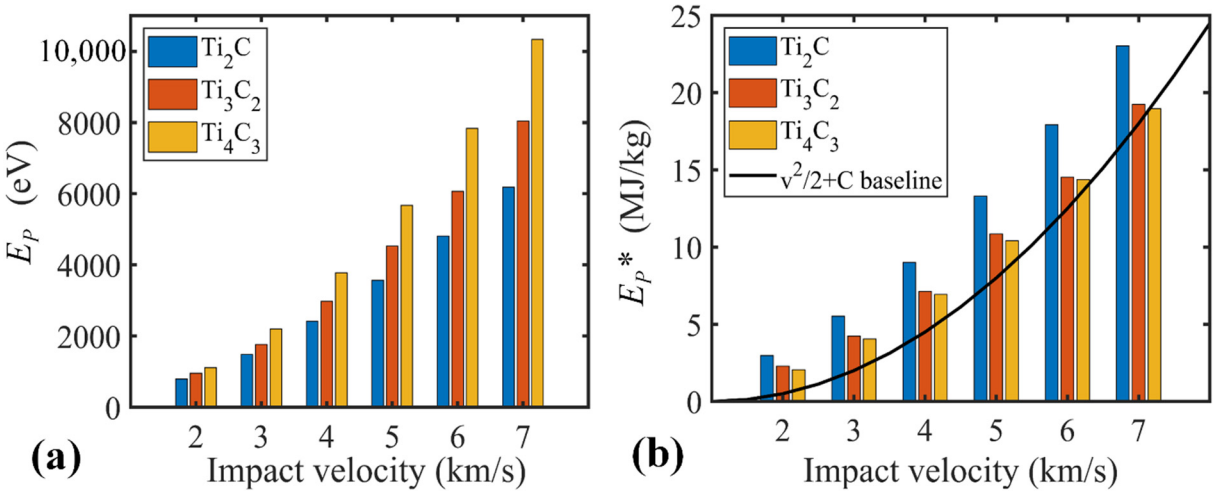

Figure 7. Performance of MXene nanosheets impact with the projectile of various velocity amplitudes. (**a**) Penetration energy and (**b**) specific penetration energy as a function of impact velocity for Ti_2C, Ti_3C_2 and Ti_4C_3 nanosheets.

For nanosheets with a thickness h far less than the projectile diameter D (i.e., $D/h >> 1$) [20], the nanosheet can be treated as a thin film, and its penetration energy can be estimated from $E_p = (\rho A_s h)v^2/2 + E_d$. The first term refers to the minimum inelastic energy or kinetic energy transferred to the target nanosheet (where A_s represents the strike face area and v stands for the impact velocity). The second term E_d represents other energy dissipation mechanisms, such as elastic deformation and the break of bonds. Further, the specific or gravimetric penetration energy that is defined as $E_p^* = E_p/(\rho A_s h)$ can be adopted to evaluate the impact resistance capability of different samples. The gravimetric penetration energy can be further expressed as $E_P^* = v^2/2 + E_d^*$. Apparently, E_d^* is a figure of merit

to evaluate the impact energy delocalization ability, which is dominated by the elastic wave propagation velocity. A stronger energy delocalization ability alleviates the local stress concentration within the nanosheet and thus enhances its impact resistance. As compared in Figure 7b, the estimated E_P^* of the examined samples generally follows the material-independent energy dissipation baseline (i.e., $v^2/2$). Under low impact velocities (<2 km/s), Ti_2C exhibits higher E_P^*, which is anticipated to be caused by the significant local deformation prior to the bond break (Figure 4). Such observation is affirmed by the energy break down shown in Figure 8, from which the potential energy increase for the Ti_2C nanosheet is comparable with the kinetic energy. As the impact velocity increases above 3 km/s, the elastic wave propagation velocity or energy delocalization ability become less dominant in determining the impact resistance ability of the nanosheet, due to the severe local deformation in the contact region (Figure 5). Different $Ti_{n+1}C_n$ MXene nanosheets share a similar Young's modulus [10,43], while the Ti_2C nanosheet has the lowest mass. Such fact makes Ti_2C exhibit a higher specific penetration energy than the other two counterparts, and the advantage becomes more evident under higher impact velocities (Figure 7b).

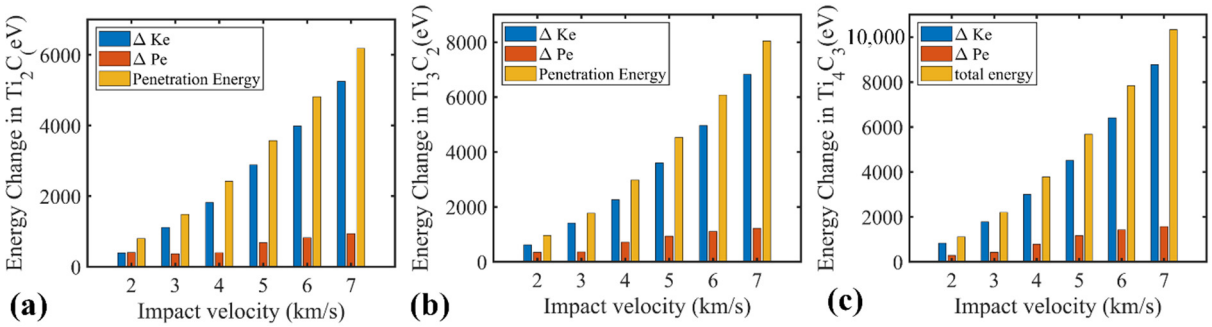

Figure 8. Energy profile of the MXene nanosheet down for (**a**) Ti_2C; (**b**) Ti_3C_2; (**c**) Ti_4C_3. The blue, orange and yellow bar represent the kinetic energy gain, potential energy gain and penetration energy, respectively.

4. Conclusions

In summary, the fracture behaviors of monolayer $Ti_{n+1}C_n$ MXene nanosheets subject to various impact velocities are explored. For low impact velocities less than 1 km/s, all of the tested samples experience significant deformation, suggesting elastic behavior. After increasing the impact velocity above its penetration threshold, Ti_2C presents the most significant out-of-plane deformation prior to perforation, followed by Ti_3C_2 and Ti_4C_3 which is consistent with the ranking of elastic wave propagation velocities. Elastic wave propagation velocity is an important figure in impact resistance assessment, as it positively correlates with the energy delocalization rate, which helps materials to deform more and thus absorb more energy prior to the bond break. As can be seen by tracking the atomic Von Mises stress distribution, Ti_2C possesses the most significant elastic wave propagation velocities, which are calculated to be 10.21 and 10.81 km/s for the X and Y direction, respectively. Though Ti_4C_3 shows an advantage in E_p among the test samples, Ti_2C nanosheets present superior E_P^* for all the tested velocity amplitudes, which indicates a negative correlation between E_P^* and the number n in the formula $Ti_{n+1}C_n$. This study provides a fundamental understanding of the deformation and penetration mechanisms of $Ti_{n+1}C_n$ nanosheets under impact, which should shed light on the design of MXenes-related composites for bullet-proof application or shielding structures for aerospace systems protection applications for $Ti_{n+1}C_n$-related composites. These results of $Ti_{n+1}C_n$ MXene nanosheets were obtained under a temperature of 10K or failure mechanisms under a higher temperature. Large-scale monolithic $Ti_{n+1}C_n$ MXene nanosheets still deserve further investigation.

Author Contributions: Conceptualization, K.X. and H.Z.; methodology, K.X.; software, K.X.; validation, K.X. and H.Z.; formal analysis, K.X.; data curation, K.X.; writing—original draft preparation, K.X.; writing—review and editing, K.X., H.Z. and X.Z.; visualization, K.X.; supervision, Z.L. All authors have read and agreed to the published version of the manuscript.

Funding: This research was funded by the National Natural Science Foundation of China (12102127, 51905150, 12172325), the Natural Science Foundation of Jiangsu Province (BK20190164), the Zhejiang Provincial Natural Science Foundation (LR22A020006), the Fundamental Research Funds for the Central Universities (B210202125) and the China Postdoctoral Science Foundation (2021M690872).

Institutional Review Board Statement: Not applicable.

Informed Consent Statement: Not applicable.

Data Availability Statement: The data presented in this study are available in this article.

Acknowledgments: The High-Performance Computer resources provided by the Queensland University of Technology are gratefully acknowledged.

Conflicts of Interest: The authors declare no conflict of interest.

References

1. Fu, Z.H.; Zhang, Q.F.; Legut, D.; Si, C.; Germann, T.C.; Lookman, T.; Du, S.Y.; Francisco, J.S.; Zhang, R.F. Stabilization and strengthening effects of functional groups in two-dimensional titanium carbide. *Phys. Rev. B* **2016**, *94*, 104103. [CrossRef]
2. Naguib, M.; Kurtoglu, M.; Presser, V.; Lu, J.; Niu, J.; Heon, M.; Hultman, L.; Gogotsi, Y.; Barsoum, M.W. Two-dimensional nanocrystals produced by exfoliation of Ti3 AlC2. *Adv. Mater.* **2011**, *23*, 4248–4253. [CrossRef] [PubMed]
3. Zhong, Y.; Xia, X.; Shi, F.; Zhan, J.; Tu, J.; Fan, H.J. Transition Metal Carbides and Nitrides in Energy Storage and Conversion. *Adv. Sci.* **2016**, *3*, 1500286. [CrossRef] [PubMed]
4. Kurtoglu, M.; Naguib, M.; Gogotsi, Y.; Barsoum, M.W. First principles study of two-dimensional early transition metal carbides. *MRS Commun.* **2012**, *2*, 133–137. [CrossRef]
5. Borysiuk, V.N.; Mochalin, V.N.; Gogotsi, Y. Bending rigidity of two-dimensional titanium carbide (MXene) nanoribbons: A molecular dynamics study. *Comput. Mater. Sci.* **2018**, *143*, 418–424. [CrossRef]
6. Hatam-Lee, S.M.; Esfandiar, A.; Rajabpour, A. Mechanical behaviors of titanium nitride and carbide MXenes: A molecular dynamics study. *Appl. Surf. Sci.* **2021**, *566*, 150633. [CrossRef]
7. Li, Z.-K.; Liu, Y.; Li, L.; Wei, Y.; Caro, J.; Wang, H. Ultra-thin titanium carbide (MXene) sheet membranes for high-efficient oil/water emulsions separation. *J. Membr. Sci.* **2019**, *592*, 117361. [CrossRef]
8. Lei, Y.; Zhao, W.; Zhang, Y.; Jiang, Q.; He, J.H.; Baeumner, A.J.; Wolfbeis, O.S.; Wang, Z.L.; Salama, K.N.; Alshareef, H.N. A MXene-Based Wearable Biosensor System for High-Performance In Vitro Perspiration Analysis. *Small* **2019**, *15*, e1901190. [CrossRef]
9. Fan, Y.; Li, L.; Zhang, Y.; Zhang, X.; Geng, D.; Hu, W. Recent Advances in Growth of Transition Metal Carbides and Nitrides (MXenes) Crystals. *Adv. Funct.* **2022**, *32*, 2111357. [CrossRef]
10. Borysiuk, V.N.; Mochalin, V.N.; Gogotsi, Y. Molecular dynamic study of the mechanical properties of two-dimensional titanium carbides Tin+1Cn (MXenes). *Nanotechnology* **2015**, *26*, 265705. [CrossRef]
11. Abraham, B.M.; Parey, V.; Singh, J.K. A strategic review of MXenes as emergent building blocks for future two-dimensional materials: Recent progress and perspectives. *J. Mater. Chem. C* **2022**, *10*, 4096–4123. [CrossRef]
12. Chu, K.; Wang, F.; Wang, X.-H.; Li, Y.-B.; Geng, Z.-R.; Huang, D.-J.; Zhang, H. Interface design of graphene/copper composites by matrix alloying with titanium. *Mater. Des.* **2018**, *144*, 290–303. [CrossRef]
13. Liu, X.; Wang, F.; Wang, W.; Wu, H. Interfacial strengthening and self-healing effect in graphene-copper nanolayered composites under shear deformation. *Carbon* **2016**, *107*, 680–688. [CrossRef]
14. Liu, X.Y.; Wang, F.C.; Wu, H.A.; Wang, W.Q. Strengthening metal nanolaminates under shock compression through dual effect of strong and weak graphene interface. *Appl. Phys. Lett.* **2014**, *104*, 231901. [CrossRef]
15. Steve, P. Fast parallel algorithms for short-range molecular dynamics. *J. Comput. Phys.* **1995**, *117*, 1–19.
16. Xia, K.; Zhan, H.; Ji, A.; Shao, J.; Gu, Y.; Li, Z. Graphynes: An alternative lightweight solution for shock protection. *Beilstein J. Nanotechnol.* **2019**, *10*, 1588–1595. [CrossRef]
17. Xia, K.; Zhan, H.; Hu, D.; Gu, Y. Failure mechanism of monolayer graphene under hypervelocity impact of spherical projectile. *Sci. Rep.* **2016**, *6*, 33139. [CrossRef]
18. Haque, B.Z.G.; Chowdhury, S.C.; Gillespie, J.W. Molecular simulations of stress wave propagation and perforation of graphene sheets under transverse impact. *Carbon* **2016**, *102*, 126–140. [CrossRef]
19. Jain, A.; Ong, S.P.; Hautier, G.; Chen, W.; Richards, W.D.; Dacek, S.; Cholia, S.; Gunter, D.; Skinner, D.; Ceder, G.; et al. The Materials Project: A materials genome approach to accelerating materials innovation. *APL Mater.* **2013**, *1*, 011002. [CrossRef]
20. Lee, J.-H.; Loya, P.E.; Lou, J.; Thomas, E.L. Dynamic mechanical behavior of multilayer graphene via supersonic projectile penetration. *Science* **2014**, *346*, 1092–1096. [CrossRef]

21. Yoon, K.; Ostadhossein, A.; van Duin, A.C.T. Atomistic-scale simulations of the chemomechanical behavior of graphene under nanoprojectile impact. *Carbon* **2016**, *99*, 58–64. [CrossRef]
22. Fonseca, A.F.; Liang, T.; Zhang, D.; Choudhary, K.; Phillpot, S.R.; Sinnott, S.B. Graphene-Titanium Interfaces from Molecular Dynamics Simulations. *ACS Appl. Mater. Interfaces* **2017**, *9*, 33288–33297. [CrossRef] [PubMed]
23. Zhang, D.; Fonseca, A.F.; Liang, T.; Phillpot, S.R.; Sinnott, S.B. Dynamics of graphene/Al interfaces using COMB3 potentials. *Phys. Rev. Mater.* **2019**, *3*, 114002. [CrossRef]
24. Jiang, T.; Zhang, X.; Vishwanath, S.; Mu, X.; Kanzyuba, V.; Sokolov, D.A.; Ptasinska, S.; Go, D.B.; Xing, H.G.; Luo, T. Covalent bonding modulated graphene-metal interfacial thermal transport. *Nanoscale* **2016**, *8*, 10993–11001. [CrossRef] [PubMed]
25. Cingolani, J.S.; Deimel, M.; Köcher, S.; Scheurer, C.; Reuter, K.; Andersen, M. Interace between graphene and liquid Cu from molecular dynamics simulations. *J. Chem. Phys.* **2020**, *153*, 074702. [CrossRef] [PubMed]
26. Lin, F.; Xiang, Y.; Shen, H.S. Tunable Positive/Negative Young's Modulus in Graphene-Based Metamaterials. *Adv. Theory Simul.* **2021**, *4*, 2000130. [CrossRef]
27. Sha, Z.; Branicio, P.; Pei, Q.; Sorkin, V.; Zhang, Y. A modified Tersoff potential for pure and hydrogenated diamond-like carbon. *Comput. Mater. Sci.* **2013**, *67*, 146–150. [CrossRef]
28. Chen, X.; Lu, S.; Zhao, Y.; Fu, T.; Huang, C.; Peng, X. Molecular dynamic simulation on nano-indentation of NiTi SMA. *Mater. Sci. Eng. A* **2018**, *712*, 592–602. [CrossRef]
29. Song, Z.; Tang, X.; Chen, X.; Fu, T.; Zheng, H.; Lu, S. Nano-indentation and nano-scratching of pure nickel and NiTi shape memory alloy thin films: An atomic-scale simulation. *Thin Solid Film.* **2021**, *736*, 138906. [CrossRef]
30. Mylvaganam, K.; Zhang, L. Ballistic resistance capacity of carbon nanotubes. *Nanotechnology* **2007**, *18*, 475701. [CrossRef]
31. Otieno, T.; Abou-El-Hossein, K. Molecular dynamics analysis of nanomachining of rapidly solidified aluminium. *Int. J. Adv. Manuf. Tech.* **2017**, *94*, 121–131. [CrossRef]
32. Poletaev, G.M.; Zorya, I.V.; Rakitin, R.Y.; Iliina, M.A. Interatomic potentials for describing impurity atoms of light elements in fcc metals. *Mater. Phys. Mech.* **2019**, *42*, 380–388.
33. Hoover, W.G. Canonical dynamics: Equilibrium phase-space distributions. *Phys. Rev. A* **1985**, *31*, 1695. [CrossRef] [PubMed]
34. Verlet, L. Computer "experiments" on classical fluids. I. Thermodynamical properties of Lennard-Jones molecules. *Phys. Rev.* **1967**, *159*, 98. [CrossRef]
35. Zhao, H.; Aluru, N.R. Temperature and strain-rate dependent fracture strength of graphene. *J. Appl. Phys.* **2010**, *108*, 064321. [CrossRef]
36. Yi, L.; Yin, Z.; Zhang, Y.; Chang, T. A theoretical evaluation of the temperature and strain-rate dependent fracture strength of tilt grain boundaries in graphene. *Carbon* **2013**, *51*, 373–380. [CrossRef]
37. Diao, J.; Gall, K.; Dunn, M.L. Atomistic simulation of the structure and elastic properties of gold nanowires. *J. Mech. Phys. Solids* **2004**, *52*, 1935–1962. [CrossRef]
38. Yin, H.; Qi, H.J.; Fan, F.; Zhu, T.; Wang, B.; Wei, Y. Griffith Criterion for Brittle Fracture in Graphene. *Nano Lett.* **2015**, *15*, 1918–1924. [CrossRef]
39. Xia, K.; Zhan, H.; Zhang, X.; Li, Z. Graphdiyne family-tunable solution to shock resistance. *Mater. Res. Express* **2020**, *7*, 115602. [CrossRef]
40. Guo, Z.; Zhou, J.; Si, C.; Sun, Z. Flexible two-dimensional Tin+1Cn (n = 1, 2 and 3) and their functionalized MXenes predicted by density functional theories. *Phys. Chem. Chem. Phys.* **2015**, *17*, 15348–15354. [CrossRef]
41. Chakraborty, P.; Das, T.; Nafday, D.; Boeri, L.; Saha-Dasgupta, T. Manipulating the mechanical properties of Ti2C MXene: Effect of substitutional doping. *Phys. Rev. B* **2017**, *95*, 184106. [CrossRef]
42. Zhang, P.; Ma, L.; Fan, F.; Zeng, Z.; Peng, C.; Loya, P.E.; Liu, Z.; Gong, Y.; Zhang, J.; Zhang, X. Fracture toughness of graphene. *Nat. Commun.* **2014**, *5*, 3782. [CrossRef] [PubMed]
43. Zhang, N.; Hong, Y.; Yazdanparast, S.; Zaeem, M.A. Superior Structural, Elastic and Electronic Properties of 2D Titanium Nitride MXenes Over Carbide MXenes: A Comprehensive First Principles Study. *2D Mater.* **2018**, *5*, 045004. [CrossRef]
44. Hernandez, S.A.; Fonseca, A.F. Anisotropic elastic modulus, high Poisson's ratio and negative thermal expansion of graphynes and graphdiynes. *Diam. Relat. Mater.* **2017**, *77*, 57–64. [CrossRef]
45. Zhang, Y.; Pei, Q.; Wang, C. Mechanical properties of graphynes under tension: A molecular dynamics study. *Appl. Phys. Lett.* **2012**, *101*, 081909. [CrossRef]